QUANTUM CHEMISTRY

Quantum simulator to emulate lower-dimensional molecular structure

E. Sierda, X. Huang, D. I. Badrtdinov, B. Kiraly, E. J. Knol, G. C. Groenenboom, M. I. Katsnelson, M. Rösner, D. Wegner*, A. A. Khajetoorians*

Bottom-up quantum simulators have been developed to quantify the role of various interactions, dimensionality, and structure in creating electronic states of matter. Here, we demonstrated a solid-state quantum simulator emulating molecular orbitals, based solely on positioning individual cesium atoms on an indium antimonide surface. Using scanning tunneling microscopy and spectroscopy, combined with ab initio calculations, we showed that artificial atoms could be made from localized states created from patterned cesium rings. These artificial atoms served as building blocks to realize artificial molecular structures with different orbital symmetries. These corresponding molecular orbitals allowed us to simulate two-dimensional structures reminiscent of well-known organic molecules. This platform could further be used to monitor the interplay between atomic structures and the resulting molecular orbital landscape with submolecular precision.

New physical and chemical phenomena can arise when electrons in solids are confined to lower dimensions (*1*, *2*). A prominent example is graphene, in which the motion of electrons becomes relativistic, which has profound consequences on its material properties including chiral (Klein) tunneling, Zitterbewegung, relativistic collapse around charge centers, and emerging pseudomagnetic fields from inhomogeneous deformations (*3*–*6*). Because of confinement, mutual interactions between electrons can furthermore become substantial in lower-dimensional systems, often leading to new and unexpected fragile quantum states of matter such as Mott insulators, superconductivity, or spin-liquid behavior (*7*–*11*). Understanding quantitatively how these exotic quantum states of matter emerge requires understanding the detailed interplay between dimensionality, multiorbital electronic structure, and interactions.

To provide insight into interacting lower dimensional systems and to take advantage of the resultant fragile many-body states of matter, new types of tunable quantum simulators have been developed toward the bottom-up design of many-body Hamiltonians (*12*–*20*). One approach toward this end is the precise atom-by-atom creation of potential landscapes on surfaces based on scanning tunneling microscopy/spectroscopy (STM/STS) (*21*, *22*). With this approach, various artificial two-dimensional (2D) lattices have been created to emulate the single-particle band structure of Dirac and topological materials (*23*–*25*). Although the versatility of this approach is rooted in the countless geometries that can be realized, it often relies on the use of supporting bulk metallic substrates. The latter is a clear drawback in designing atomic and molecular orbitals with tailored symmetry, as well as tuning mutual electron interactions, because of the unwanted influence of the substrate's bulk electronic bands. Therefore, to harness the versatility of this approach, it is vital to develop platforms that use weakly conducting or insulating surfaces (*26*, *27*).

Here, we demonstrated a versatile quantum simulator capable of realizing complex artificial molecular orbitals based solely on patterning individual cesium (Cs) atoms on the surface of semiconducting indium antimonide (InSb). Using STM/STS, we first constructed building blocks from patterned ring structures of Cs atoms, which exhibited a zero-dimensional (0D)–like state, attributable to an artificial atom. This sharply observable bound state in the band gap of the semiconducting substrate was hence strongly decoupled from the bulk and exhibited spatially extended charge density outside the artificial atom. We subsequently showed that two artificial atoms exhibited a long-range distance-dependent coupling, leading to the formation of bonding and antibonding states. Using this as a starting point, we demonstrated the multiorbital nature of the simulator, which was based on creating artificial atomic s, p_x, and p_y orbitals. We used various orbital symmetries and constructed 2D structures with defined geometries that are reminiscent of analogous planar 3D molecular structures. The resultant electronic structure exhibited 2D artificial molecular orbitals, namely molecular σ and π orbitals, with various in-plane symmetries due to orbital hybridization. Using ab initio calculations of the analogous molecules, we compared the resultant and expected molecular orbitals. Because the tailored structures are not restricted by the geometrical relaxation of their molecular analogs, this platform provides an ultimate tool to explore fragile and degenerate states and the interplay of these states with geometrical structure. We demonstrated this by exploring 2D structures that were reminiscent of various conformations of butadiene molecules.

Artificial atoms

InSb is a semiconductor with a band gap of 235 meV (*28*). Upon adsorption on its (110) surface, Cs atoms resided at hollow sites of the Sb-terminated surface (supplementary text, section S1, and figs. S1 and S2) (*29*). Concomitantly, charge donation from Cs atoms led to band bending and a dilute 2D electron gas (2DEG), whose dimensionality has also been demonstrated through the quantum Hall effect (*30*–*33*). This 2DEG could be seen by a steplike onset in STS observed in the bulk band gap of the semiconductor (fig. S3), with a carrier density of $N_{2DEG} = 2 \times 10^{12}$ cm^{-2}, where each Cs ion donated approximately 0.4 electrons (supplementary text, section S2, and figs. S4 to S6), depending on the Cs density and doping of the semiconductor (*31*, *32*).

We exploited the ionic nature of individual Cs atoms and patterned them into ring structures (Fig. 1, A and B) to create a potential energy landscape that mimics the $1/r$ potential of an atom in two dimensions. The local concentration of Cs ions created an attractive potential for the electrons of the 2DEG, leading to a bound state within the bulk band gap that could be visualized by STS (Fig. 1, C and D). This bound state manifested as a sharp peak with full width at half maximum of FWHM ≃ 7 mV. Using spatially dependent differential conductance (dI/dV) imaging (see supplementary materials and methods) at the peak energy (Fig. 1C), which we refer to as an orbital map, we found that this bound state was not only located within the ring structure but also symmetrically delocalized up to $r = 9.0 \pm 0.4$ nm outside of the structure (fig. S7). The spatial delocalization of this wave function was due to the interplay of the local-band bending induced by the Cs ring structure and the weak screening of the 2DEG. As a result, we could identify this bound state as an s-like atomic state stemming from the circular potential, which is observable at a sufficiently large distance from the structure. We therefore defined this structure as an artificial atom. For the ring structures that we used in this manuscript, the structural deviations of the Cs atoms from circular symmetry were small compared to the length scale of the associated wave function. Consequently, such deviations led to negligible changes (e.g., anisotropy) in the electronic structure. Previously, it has also been shown that the 2DEG itself is approximately isotropic (*33*). Therefore, the resultant potential was well approximated by a circularly symmetric $1/r$ potential in the xy plane at sufficient separation from the Cs ring structure. We verified this both theoretically and by comparing different artificial Cs

Institute for Molecules and Materials, Radboud University, Nijmegen, Netherlands.
*Corresponding author. Email: a.khajetoorians@science.ru.nl (A.A.K.); d.wegner@science.ru.nl (D.W.)

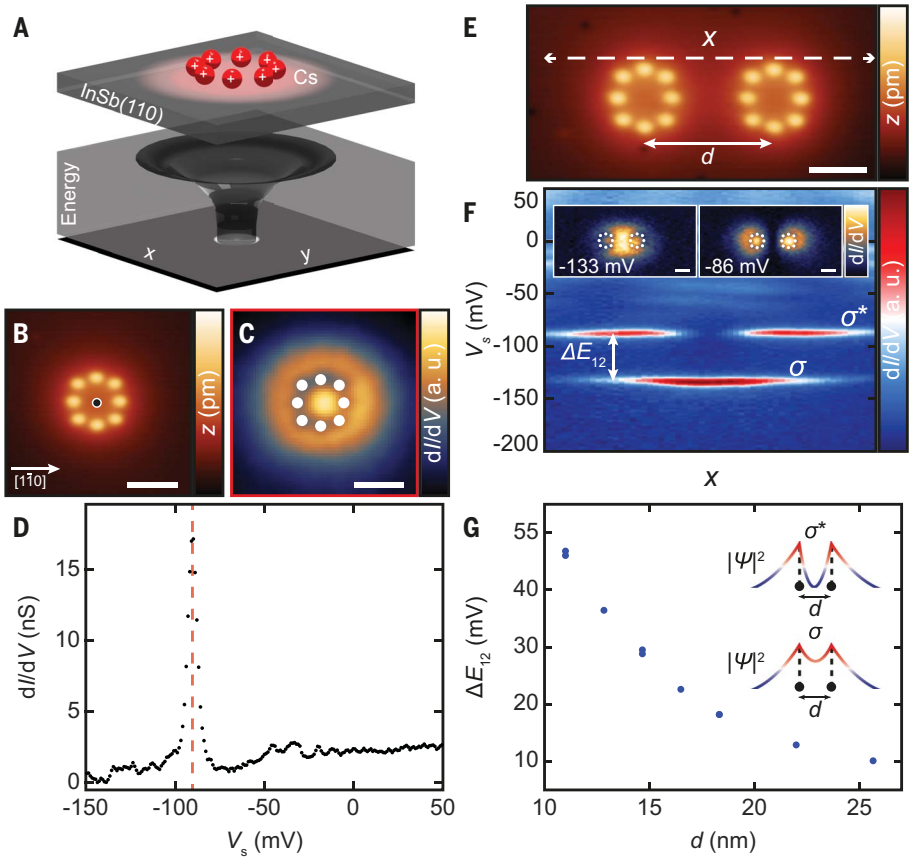

Fig. 1. Formation of an artificial atom from Cs atoms on InSb(110) and bonding/antibonding orbitals of coupled artificial atoms. (**A**) Schematic of the artificial atom created from Cs with a representation of the attractive confinement potential. (**B**) Constant-current STM image of an artificial atom derived from eight Cs atoms arranged in a ring structure (lateral scale, 5 nm; Δz = 300 pm). (**C**) Orbital map of the bound state of the artificial atom in (B), obtained at the voltage marked with a red dashed line in (D) (V_S = −91 mV). The white circles were added to represent the Cs atoms for clarity. (**D**) d*I*/d*V* spectroscopy measured at the indicated black dot in (B), revealing a bound state (red dashed line) within the bulk band gap. (**E**) Constant-current STM image of two artificial atoms separated by $d \approx 11$ nm (lateral scale, 5 nm; Δz = 300 pm). (**F**) d*I*/d*V* spectroscopy measured sequentially along the dashed white line *x* marked in (E). The σ and σ* indicate the bonding and antibonding orbitals, which are separated by ΔE_{12} = 46 mV. Insets in (F) represent spatial distribution of the bonding (σ) and antibonding (σ*) orbitals registered at V_S = −133 mV and V_S = −86 mV, respectively. The white circles were added to represent the positions of the Cs atoms for clarity. (**G**) Distance dependence of the coupling strength $\Delta E_{12}(d)$ between two artificial atoms as a function of separation *d*. The inset shows a textbook schematic representation of squared wave functions of σ and σ* orbitals. a.u., arbitrary units.

structures (supplementary texts, sections S3 and S4; figs. S7, S8, and S9). The calculations showed that the artificial atom also contained orbitals with and p_x and p_y symmetries, which were not observed experimentally because they presumably resided above the Fermi energy (E_F), within the conduction band. Because each Cs atom donated only a fraction of its outer 6*s* electron (*31*, *32*), assigning an integer number of electrons bound to the artificial atom was not possible. As a result, the mesoscopic description of an artificial atom most likely involves many-body effects. However, for distances much larger than the Cs–Cs distance within the artificial atom, we reduced the many-body problem into an effective single-particle Hamiltonian and the aforementioned $1/r$ potential, as shown in the next section.

Coupling artificial dimers

To tailor Hamiltonians that resemble molecular orbitals, it was first necessary to demonstrate that these artificial atoms can couple. We correspondingly created dimers of two artificial atoms separated by $d \approx 11$ nm (Fig. 1E), where *d* is defined as the center-to-center distance. In Fig. 1F, we illustrate a false-color plot of spatially dependent STS taken at points along the line indicated in Fig. 1E. The spectra in Fig. 1F revealed two sharp low-energy states separated by ΔE_{12} = 46.0 ± 0.6 meV. Although the lowest-energy state was most strongly localized in between the two artificial atomic sites, the higher-energy state exhibited a pronounced node with negligible intensity at the same location. Orbital maps (Fig. 1F, inset) confirmed that these energy levels could be identified as bonding (σ) and antibonding (σ*) orbitals resulting from the coupling between the two artificial atomic s orbitals. This behavior persisted for different spacings *d*, where the value of ΔE_{12} monotonically decreased for increasing *d* and was nonzero up to $d \approx 25$ nm (Fig. 1G). This distance dependence could be fitted and well described by a simple tight binding model that considers nearest-neighbor interactions and isotropic atomic orbitals. In comparison with previous observations on other surfaces (*23*–*27*, *34*), our data showed the sharpest peak widths with FWHM ≃ 8 mV, much smaller than ΔE_{12}. For a detailed discussion, see supplementary text (section S5) and fig. S10.

Higher-orbital symmetries in artificial atomic chains

Before simulating molecular orbitals, it was necessary to confirm that the coupling of artificial atomic states also leads to orbitals with distinct symmetry, such as with σ and π characters. Therefore, we fabricated a linear molecular chain composed of six artificial atoms, where each artificial atomic site is separated by $d \approx 12.8$ nm (Fig. 2A). Using d*I*/d*V* spectra taken along a line near the structure as input (fig. S11), we identified more states separated by smaller energies. To uncover the nature of these states, we acquired orbital maps (fig. S12). In the following, we provide a summary and reference supplementary text (section S6) for a more detailed discussion.

The lowest six states resembled a series of σ molecular orbitals derived from a superposition of the artificial atomic s orbitals. Following a textbook example of the linear combination of atomic orbitals (LCAO), an increasing number of nodes was found with increasing energy. We note that a simple tight-binding model using the same parameters as for the dimers and considering only nearest-neighbor hopping was sufficient to reproduce the energies of all σ orbitals. At higher energies (sample bias voltage $V_S \geq -51$ mV), we found three additional states (Fig. 2, D and E, and fig. S12I) that we identified as a series of molecular orbitals derived from LCAO-like superpositions of artificial atomic p_y orbitals, leading to artificial molecular π orbitals with a node plane along the chain axis and increasing local density of states (LDOS) above and below the chain. Again, the number of nodes along the *y* axis increased with increasing energy. Although there should still be

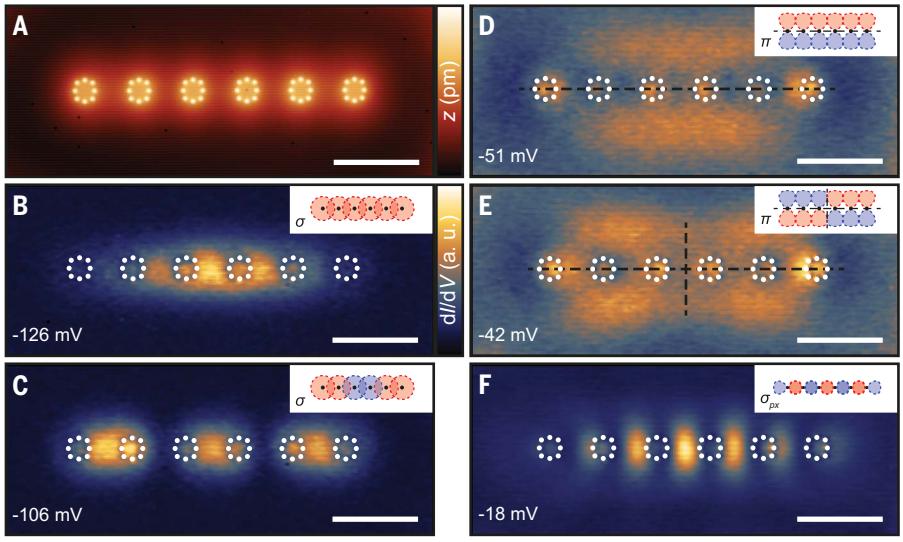

Fig. 2. Multiorbital states in an artificial molecular chain. (**A**) Constant-current STM image of a linear chain composed of six artificial atoms with equal separation $d \approx 12.8$ nm (V_S = 50 mV; lateral scale, 20 nm; Δz = 300 pm). (**B** to **F**) Orbital maps obtained at the voltages indicated in lower-left corner of each image (z_{offset} = −140 pm; V_{mod} = 2 mV; lateral scale, 20 nm). The white circles represent the Cs atomic positions. A schematic representation of atomic-like orbital contributions is provided in the inset of each map, where red and blue colors represent a positive or negative sign of the depicted wave function, respectively. [(B) and (C)] Two σ orbitals: first and third. [(D) and (E)] Set of two π orbitals. Black lines indicate the location of the nodal planes. (F) σ orbital originating from artificial atomic p_x orbitals. a.u., arbitrary units.

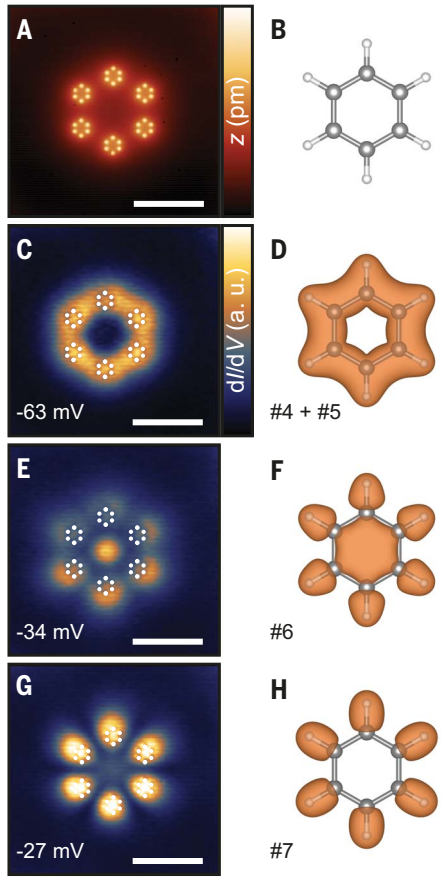

Fig. 3. Artificial benzene and its orbital structure. (**A**) Constant-current STM image of six artificial atoms arranged into a benzene structure with separation of $d \approx 10.5$ nm (lateral scale, 20 nm; Δz = 300 pm). (**B**) The ball-stick model for the benzene molecule in the DFT calculations. (**C**, **E**, **G**) Orbital maps obtained at the voltages indicated in the lower-left corner of each image (z_{offset} = −140 pm;, V_{mod} = 2 mV; lateral scale, 20 nm). The white circles were added to represent the Cs atoms for clarity. (**D**, **F**, **H**) Set of benzene VMOs obtained from the DFT calculations corresponding to orbital maps on the left. The calculations represent the charge density and include the summed charge densities for degenerate orbitals in (D). The orbital order number is indicated in the lower-left corner of each image. a.u., arbitrary units.

three more p_y-derived molecular orbitals at higher sample biases, we did not observe them, presumably because they were located at energies where hybridization with the conduction band may have weakened and broadened their LDOS. However, we found another σ orbital at V_S = −18 mV (Fig. 2F), which perfectly resembled the LCAO of artificial atomic p_x orbitals with bonding character, leading to increased LDOS along the chain axis between each of the artificial atomic sites.

As the form of the potential into the bulk of the InSb can be approximated as a triangular-well potential (*30*), artificial atomic orbitals of p_z-like character cannot be emulated, limiting the dimensionality that can be explored. Accordingly, we did not discover any orbital of p_z-like character in any of our artificial molecular structures. In two dimensions, p_z orbitals project onto s orbitals, which is why many electronic properties of 2D materials originating from p_z-derived bands should also be observable in a pure 2D system. Moreover, evidence for π-like orbitals has previously been reported in an artificial structure (*35*), albeit orbital maps, as done here, are necessary to distinguish different orbital symmetries.

Artificial hybrid molecular orbitals

As a final step toward emulating molecular orbitals, it was necessary to show that artificial atomic orbitals can hybridize. We therefore subsequently created a six-fold symmetric hexagon of artificial atoms, each composed of six Cs atoms, reminiscent of a benzene ring (Fig. 3A; see fig. S14 for structural details). We chose to use a six-Cs structure to permit faster assembly of artificial structures containing many artificial atoms, noting that it also exhibited an *s*-like state and qualitatively did not differ from the eight-Cs structure (supplementary text, sections S4 and S11; figs. S9, S31, and S32). To identify resonance energies, we acquired STS spectra at various locations (fig. S15) and subsequently imaged the resultant orbital maps (*36*). An excerpt of the maps is presented in Fig. 3 and compared with density functional theory (DFT) calculations of the actual benzene molecule. For a detailed identification and discussion of all states, we refer to the supplementary text (section S7) and figs. S13 to S16. In short, for energies below E_F, we could connect all but one of the orbital maps with the first eight calculated benzene valence molecular orbitals (VMOs) by comparing the experimental dI/dV intensities with the calculated charge densities at scaled distances. In cases of degenerate VMOs, we compared their superposition with the experimental maps. The overall qualitative agreement between the orbital maps and the calculated molecular orbitals provided evidence that the artificial atomic s, p_x, and p_y orbitals have undergone sp^2 hybridization to form artificial molecular orbitals.

The versatility of this platform allowed us to create lower-dimensional structures with fragile low-energy states and interrogate the role of geometry on these states. Although the simulated structures are not one-to-one identical to their molecular analogs (e.g., see the discussion regarding p_z orbitals above), studying this interplay is not easily possible in real molecular systems because of other restricting effects, such as relaxation. As an example of this versatility, we built 2D structures which were inspired by real 3D molecules that have nearly degenerate ground states and are hence unstable, and we constructed and compared

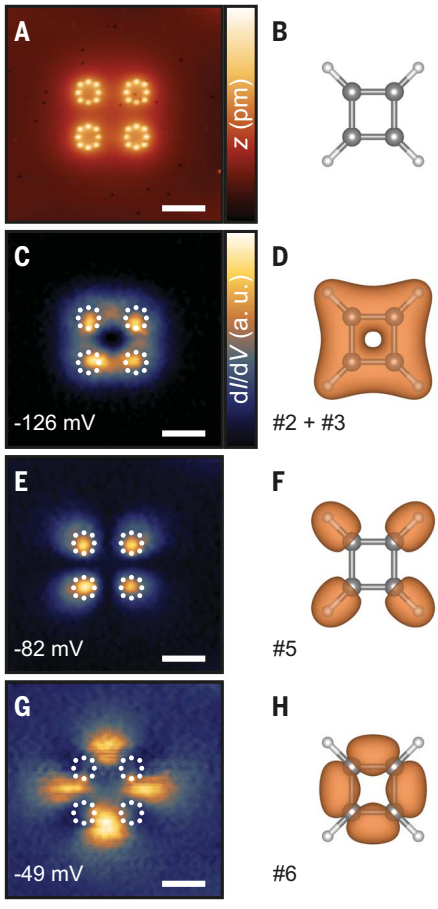

Fig. 4. Artificial cyclobutadiene and its orbital structure. (**A**) Constant-current STM image of four artificial atoms arranged in a cyclobutadiene structure with $d \approx 11$ nm (lateral scale, 10 nm; $\Delta z = 300$ pm). (**B**) The ball-stick model used for the cyclobutadiene molecule in the DFT calculations. (**C**, **E**, **G**) Set of orbital maps obtained at voltages indicated in the lower-left corner of each image. The white circles were added to represent the Cs atoms for clarity ($z_{offset} = -100$ pm; $V_{mod} = 1$ mV; lateral scale, 10 nm). (**D**, **F**, **H**) Set of cyclobutadiene VMOs obtained from the DFT calculations corresponding to orbital maps on the left. The calculations represent the charge density and include the summed charge densities for degenerate orbitals in (D). The orbital order number is indicated in the lower-left corner of each image. a.u., arbitrary units.

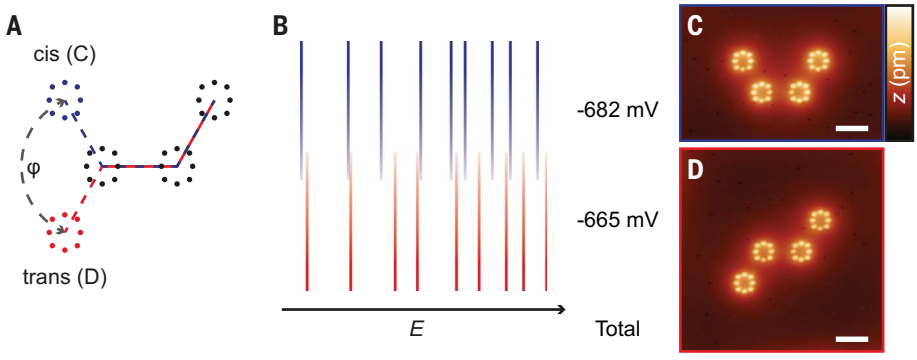

Fig. 5. Comparison of artificial *cis*- and *trans*-butadiene. (**A**) Schematic model of the artificial molecular structure built from four artificial atoms in both cis and trans conformations. (**B**) Schematic comparison of the energies of all nine orbitals from the ground state up to E_F of the cis (blue) and trans conformer (red) as identified from STS. The total energy is the sum of these eigenenergies. (**C** and **D**) Constant-current STM image of (C) the cis and (D) the trans conformer (lateral scale, 10 nm; $\Delta z = 300$ pm).

2D analogs of conformational isomers. We subsequently present examples inspired by various structural realizations of butadiene. For simplicity, we refer to these structures as artificial butadiene.

We started by coupling four artificial atoms separated by $d \approx 11$ nm that form a nearly square arrangement (Fig. 4A; see fig. S19 for details of the structure), resembling the core of cyclobutadiene (Fig. 4B). From simple molecular orbital theory and Hückel's rule, cyclobutadiene in a fourfold symmetric geometry would be antiaromatic and unstable, and it undergoes a Jahn-Teller distortion (*37*, *38*). We applied the same approach as used for artificial benzene above to identify and map the artificial molecular orbitals, which we compared with DFT-calculated orbitals of actual cyclobutadiene in its fourfold-symmetric form (Fig. 4, C and H). For a detailed identification and discussion of all states, we refer to the supplementary text (section S8) and figs. S18 to S22. In short, we were able to assign the first five orbital maps to the first six calculated VMOs of cyclobutadiene. The maps at −67 mV and −49 mV exhibited some deviations, particularly a blurred distribution with reduced intensity. We speculate that this effect can be caused by the orbitals coupling to the 2DEG, which would delocalize the LDOS. Furthermore, small asymmetries were visible, presumably because the structure deviated from a perfect fourfold symmetry (fig. S19), but with no noticeable anisotropy on the orbital levels (fig. S20). Our simulator allows us to explore the interplay of the resultant electronic structure of analogous 2D structures, with or without such distortions.

In a similar fashion as for the cyclobutadiene structure, we also built artificial structures inspired by the cis and trans conformers of 1,3-butadiene, as schematically shown in Fig. 5A (for details, see supplementary text, sections S9 and S10, and figs. S23 to S30). We first built the cis conformer (Fig. 5C) and identified all orbital maps from STS and comparison with calculations. Then, we repositioned the same group of Cs atoms of the left-hand artificial atom to build the trans conformer (Fig. 5D), and we repeated all spectroscopic measurements and calculations. This way, as we built both structures using the same Cs atoms on the same surface with the same local environment, we ensured that the acquired energies are directly comparable. The schematic energy-level diagram of all nine molecular orbitals found below E_F (Fig. 5B) shows that the levels of the cis conformer overall tended to be a bit lower, leading to a reduced sum of the occupied-state energies $E^{cis}_{total} = -682$ meV compared with $E^{trans}_{total} = -665$ meV. In the real 1,3-butadiene molecule, the cis conformer has a higher energy because of steric hindrance, leading to structural bending out of the 2D plane (*39*), which emphasizes both limitations and differences between our lower-dimensional platform and analog 3D molecules. However, as an advantage, this platform would enable to change the angle ϕ quasicontinuously, allowing us to experimentally map the potential landscape against this "reaction coordinate," hence providing a quantitative Walsh diagram for our artificial structure (*40*). Furthermore, equal versus alternating bond lengths can be compared to understand the impact of bond order in this artificial platform.

To showcase the versatility and expandability of our quantum simulator, we also built larger artificial structures representing a transition toward extended lattices. As an example, we manipulated 132 Cs atoms into a network of 22 artificial atoms arranged in a structure that is reminiscent of triangulene (supplementary text, section S12, and figs. S32 to S36), a molecule that is difficult to synthesize and has most recently drawn attention owing to its unusual electron and spin configurations (*41*–*46*).

There are several interesting observations that raise questions about the respective physical origin. For example, there is an uncanny resemblance between VMOs of organic molecules and the 2D orbital maps of the artificial structures built here. Similarly, there is an open question as to which artificial site can be related to an actual element in terms of electron occupation (e.g., C or H) and whether artificial heterostructures (i.e., resembling different elements) can be realized. Related to

this, the link between gating these artificial structures and emulating charge transfer may show exciting prospects. Finally, there are distinct differences related to the dimensionality of the platform, namely that it is below 3D, and comparisons to 3D molecular structure. We discuss these points further in the supplementary text (sections S13 and S14) and in figs. S37 and S38.

Conclusion

We have developed a versatile solid-state quantum simulator based on the use of Cs ions embedded in a 2DEG on the surface of semiconducting InSb(110). We showed that artificial atoms can be created with an electronic signature given by a sharp bound state in the semiconductor band gap. The coupling of the generated electronic states with the bulk is strongly suppressed, leading to charge densities that are spatially delocalized over distances much larger than an expected atomic wave function. This leads to long-range coupling and the ability to create artificial atomic and molecular orbitals with different symmetries. On the basis of this, we created a variety of lower-dimensional structures, from dimers to chains and eventually structures that resemble common organic molecules, and characterized their low-energy electronic structure. We found an uncanny resemblance between the expected in-plane VMOs, as calculated with DFT of the free-standing molecule, and the measured orbital energic order and structure of the artificial molecules. Moreover, we showed that well-known conformational isomers can be artificially simulated, and the geometry perturbed, where the changes in electronic structure as a function of structural change can be monitored. The versatility of the platform is based on being able to create fragile structures with degeneracy, which are often dominated by structural relaxations (e.g., Jahn-Teller distortion), and probe the interplay between geometry and the resultant electronic structure. This approach is distinctly different from that of previous studies of artificial lattices in which utilized states are strongly coupled to the bulk (*21*–*25*, *34*, *47*); for example, the use of scattered quasiparticles from patterned defects on metallic surfaces. At large distance, the attractive potential can be approximated as an atomic-like $1/r$ potential, but locally, the description involving the Cs ions and local 2D carriers most likely involved many-body interactions (*48*). In this way, owing to the interplay of poor screening, lower dimensionality, and low carrier density, this platform may also be suitable for exploring tailored many-body states in designed structures based on strong electron-electron interactions.

REFERENCES AND NOTES

1. D. Deng *et al*., *Nat. Nanotechnol.* **11**, 218–230 (2016).
2. K. S. Novoselov *et al*., *Nature* **438**, 197–200 (2005).
3. M. I. Katsnelson, *The Physics of Graphene* (Cambridge Univ. Press, ed. 2, 2020).
4. M. I. Katsnelson, K. S. Novoselov, A. K. Geim, *Nat. Phys.* **2**, 620–625 (2006).
5. N. Levy *et al*., *Science* **329**, 544–547 (2010).
6. Y. Wang *et al*., *Science* **340**, 734–737 (2013).
7. L. Perfetti *et al*., *Phys. Rev. Lett.* **90**, 166401 (2003).
8. Y. Chen *et al*., *Nat. Phys.* **16**, 218–224 (2020).
9. X. Xi *et al*., *Nat. Nanotechnol.* **10**, 765–769 (2015).
10. P. Dreher *et al*., *ACS Nano* **15**, 19430–19438 (2021).
11. K. T. Law, P. A. Lee, *Proc. Natl. Acad. Sci. U.S.A.* **114**, 6996–7000 (2017).
12. Y. Cao *et al*., *Nature* **556**, 43–50 (2018).
13. Y. Cao *et al*., *Nature* **556**, 80–84 (2018).
14. A. A. Houck, H. E. Türeci, J. Koch, *Nat. Phys.* **8**, 292–299 (2012).
15. I. Bloch, *Nat. Phys.* **1**, 23–30 (2005).
16. I. Bloch, J. Dalibard, S. Nascimbène, *Nat. Phys.* **8**, 267–276 (2012).
17. R. Blatt, C. F. Roos, *Nat. Phys.* **8**, 277–284 (2012).
18. D. S. Lühmann, C. Weitenberg, K. Sengstock, *Phys. Rev. X* **5**, 031016 (2015).
19. C. Gross, I. Bloch, *Science* **357**, 995–1001 (2017).
20. A. Singha *et al*., *Science* **332**, 1176–1179 (2011).
21. A. A. Khajetoorians, D. Wegner, A. F. Otte, I. Swart, *Nat. Rev. Phys.* **1**, 703–715 (2019).
22. M. F. Crommie, C. P. Lutz, D. M. Eigler, *Science* **262**, 218–220 (1993).
23. K. K. Gomes, W. Mar, W. Ko, F. Guinea, H. C. Manoharan, *Nature* **483**, 306–310 (2012).
24. M. R. Slot *et al*., *Nat. Phys.* **13**, 672–676 (2017).
25. R. Drost, T. Ojanen, A. Harju, P. Liljeroth, *Nat. Phys.* **13**, 668–671 (2017).
26. S. Fölsch, J. Martínez-Blanco, J. Yang, K. Kanisawa, S. C. Erwin, *Nat. Nanotechnol.* **9**, 505–508 (2014).
27. Y. Pan, J. Yang, S. C. Erwin, K. Kanisawa, S. Fölsch, *Phys. Rev. Lett.* **115**, 076803 (2015).
28. I. Vurgaftman, J. R. Meyer, L. R. Ram-Mohan, *J. Appl. Phys.* **89**, 5815–5875 (2001).
29. L. J. Whitman, J. A. Stroscio, R. A. Dragoset, R. J. Celotta, *Phys. Rev. Lett.* **66**, 1338–1341 (1991).
30. K. Hashimoto *et al*., *Phys. Rev. Lett.* **101**, 256802 (2008).
31. S. Becker, M. Liebmann, T. Mashoff, M. Pratzer, M. Morgenstern, *Phys. Rev. B Condens. Matter Mater. Phys.* **81**, 155308 (2010).
32. S. Becker *et al*., *Phys. Rev. Lett.* **106**, 156805 (2011).
33. M. Morgenstern *et al*., *Physica E* **44**, 1795–1814 (2012).
34. W. Jolie *et al*., *ACS Nano* **16**, 4876–4883 (2022).
35. V. D. Pham, K. Kanisawa, S. Fölsch, *Phys. Rev. Lett.* **123**, 066801 (2019).
36. J. Repp, G. Meyer, S. M. Stojković, A. Gourdon, C. Joachim, *Phys. Rev. Lett.* **94**, 026803 (2005).
37. T. Bally, S. Masamune, *Tetrahedron* **36**, 343–370 (1980).
38. A. Kostenko *et al*., *Angew. Chem. Int. Ed.* **56**, 10183–10187 (2017).
39. D. Feller, N. C. Craig, *J. Phys. Chem. A* **113**, 1601–1607 (2009).
40. A. D. Walsh, *J. Chem. Soc.* 2260–2266 (1953).
41. E. Clar, D. G. Stewart, *J. Am. Chem. Soc.* **75**, 2667–2672 (1953).
42. J. Inoue *et al*., *J. Am. Chem. Soc.* **123**, 12702–12703 (2001).
43. S. Mishra *et al*., *Angew. Chem. Int. Ed.* **59**, 12041–12047 (2020).
44. S. Mishra *et al*., *Nature* **598**, 287–292 (2021).
45. N. Pavliček *et al*., *Nat. Nanotechnol.* **12**, 308–311 (2017).
46. M. Randić, *Chem. Rev.* **103**, 3449–3605 (2003).
47. M. R. Slot *et al*., *Phys. Rev. X* **9**, 011009 (2019).
48. F. Ma *et al*., *Phys. Rev. X* **10**, 031058 (2020).
49. E. Sierda *et al*., Data for "Quantum simulator to emulate lower dimensional molecular structure." Radboud Data Repository (2023); https://doi.org/10.34973/faps-jp08.

ACKNOWLEDGMENTS

Funding: The experimental part of this project was supported by the European Research Council (ERC) under the European Union's Horizon 2020 research and innovation program (grant no. 818399). We also acknowledge support from the NWO-VIDI project "Manipulating the interplay between superconductivity and chiral magnetism at the single-atom level" with project no. 680-47-534. B.K. acknowledges the NWO-VENI project "Controlling magnetism of single atoms on black phosphorus" with project no. 016.Veni.192.168. The work of M.I.K. was supported by the ERC under the European Union's Horizon 2020 research and innovation program (grant no. 854843-FASTCORR). This publication is part of the project TOPCORE (project no. OCENW.GROOT.2019.048) of the research program Open Competition ENW Groot, which is partly financed by the Dutch Research Council (NWO). **Author contributions:** E.S., X.H., B.K., and E.J.K. performed the experiments. D.I.B., M.I.K., and M.R. performed the DFT and model calculations, with input from G.C.G. including supplemental quantum chemical calculations. E.S., X.H., D.I.B., G.C.G., M.I.K., M.R., D.W., and A.A.K. performed and discussed the data analysis. G.C.G., D.W., and A.A.K. designed the experiments. All authors contributed to the writing of the manuscript and scientific discussion. **Competing interests:** The authors declare no competing interests. **Data and materials availability:** All data needed to evaluate the conclusions in the paper are present in the paper or the supplementary materials. Data for all figures presented in this study are available at Radboud Data Repository (*49*). The following software was used: Gwyddion 2.60 and Matlab R2022a (data processing), VESTA 3.5.7 (visualization of DFT calculations), and Blender 3.3.1 and Adobe Illustrator 27.1 (figure preparation and 3D rendering).

This research was funded in whole or in part by NWO (680-47-534, 016.Veni.192.168, and OCENW.GROOT.2019.048), a cOAlition S organization. The authors will make the Author Accepted Manuscript (AAM) version available under a CC BY public copyright license.

SUPPLEMENTARY MATERIALS

science.org/doi/10.1126/science.adf2685
Materials and Methods
Supplementary Text
Figs. S1 to S38
Table S1
References (*50*–*59*)

Submitted 10 October 2022; resubmitted 22 February 2023
Accepted 10 May 2023
10.1126/science.adf2685